Improving Electronic Conductivity of Layered Oxides through the Formation of Two-Dimensional Heterointerface for Intercalation Batteries

Mallory Clites, Ryan Andris, David A. Cullen, Karren L. More, and Ekaterina Pomerantseva*

Read Online

ACCESS | Metrics & More | Article Recommendations | Supporting Information

ABSTRACT: Synthetic strategies for the improvement in electronic conductivities and electrochemical stabilities of transition metal oxide cathodes, which are limiting factors in the performance of commercial intercalation batteries, are required for next-generation, high-performance battery systems. The chemical preintercalation approach, consisting of a combined sequence of a sol−gel process, extended aging, and a hydrothermal treatment, is a versatile, wet synthesis technique that allows for the incorporation of a polar species between the layers of transition metal oxides. Here, formation of a layered 2D δ-$C_xV_2O_5 \cdot nH_2O$ heterostructure occurs via chemical preintercalation of dopamine molecules between bilayers of vanadium oxide followed by the hydrothermal treatment of the precipitate, leading to carbonization of the organic molecules. The presence of carbon layers within the structure has been confirmed via a combined analysis of scanning electron microscopy, X-ray diffraction, thermogravimetric analysis, Raman spectroscopy, X-ray photoelectron spectroscopy, electrochemical impedance spectroscopy, four-probe conductivity measurements, and scanning transmission electron microscopy characterization. 2D δ-$C_xV_2O_5 \cdot nH_2O$ heterostructure electrodes demonstrated significantly improved electrochemical performance, particularly at higher current densities, in Li-ion cells. The heterostructure electrodes exhibited 75% of the capacity retention when the current was changed from 20 mA g^{-1} (206 mAh g^{-1}) to 300 mA g^{-1} (155 mAh g^{-1}), while the reference δ-$V_2O_5 \cdot nH_2O$ electrodes exhibited only 10% capacity retention in the same experiment. Remarkably, 2D δ-$C_xV_2O_5 \cdot nH_2O$ heterostructure electrodes demonstrated significantly improved capacity retention (94% after 30 cycles) for bilayered vanadium oxide electrodes in Li-ion cells during galvanostatic cycling at 20 mA g^{-1}. The improved electrochemical performance, in both extended cycling and rate capability studies, of the 2D δ-$C_xV_2O_5 \cdot nH_2O$ heterostructure electrodes in the Li-ion system is ascribed to the intermittent formation of carbon layers within the bilayered structure, which leads to increased electronic conductivity and improved structural stability of the heterostructure compared to the reference δ-$V_2O_5 \cdot nH_2O$ electrodes.

KEYWORDS: chemical preintercalation synthesis approach, bilayered vanadium oxide, two-dimensional heterostructures, carbonization, Li-ion batteries
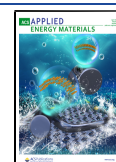
INTRODUCTION

The expanding variety of applications relying on portable autonomous power calls for innovative energy storage solutions with high performance. The performance of lithium-ion batteries (LIBs), the most widely used energy storage system today, is limited by the availability of cathode materials. Layered transition metal oxides show high redox activity in intercalation reactions and relatively high working potentials, making them especially attractive for use as cathodes in batteries. In commercial LIBs used today, the cathodes are typically made of layered transition metal oxides, such as lithium cobalt oxide ($LiCoO_2$ or LCO), lithium nickel cobalt aluminum oxide (commonly $LiNi_{0.8}Co_{0.15}Al_{0.05}O_2$ or NCA), and lithium nickel cobalt manganese oxide (often $LiNi_{0.6}Co_{0.2}Mn_{0.2}O_2$ or $LiNi_{0.8}Co_{0.1}Mn_{0.1}O_2$ or NCM).[1,2]

However, the low electronic conductivity of most oxides limits their performance. Moreover, the distance between the structural layers in these materials does not exceed 5 Å, and more open two-dimensional (2D) diffusion channels are needed to achieve fast ion transport. Expanding the interlayer region combined with incorporation of the transition metal ions with high oxidation states such as V^{5+}, Nb^{5+}, Mo^{6+}, or W^{6+}

in the structural layers can be an effective strategy to increase the specific capacity of the cathodes in intercalation batteries— a long sought after capability needed to realize batteries with higher energy densities compared to the performance characteristics achievable today. Utilizing such materials with high operating voltage/specific capacity and fast ion/electron transport as intercalation battery cathodes is attractive for creating next-generation batteries with high energy and power density.

An oxide material that meets both the requirement of forming a layered structure with expanded interlayer spacing and containing a transition metal ion in the high oxidation state within the layers is bilayered (or δ-) vanadium oxide.[3] The 2D bilayered V_2O_5 slabs are separated by a large interlayer spacing of 11.5 Å stabilized by structural water, which is unusual for an oxide. It was shown that δ-$V_2O_5 \cdot nH_2O$ delivers high specific capacities in both LIB and beyond lithium ion (BLI) energy storage systems.[4−17] However, bilayered vanadium oxide electrodes exhibited moderate rate performance, which was attributed to the low electronic conductivity and is typical for most oxides. To overcome this limitation, layered oxides can be combined with layers of electronically conductive 2D materials, such as carbon-based compounds, by alternating layers of dissimilar materials to stack them into a 2D heterostructure.[18] The nanoscale size of 2D heterostructures can further facilitate transport of ions and electrons, thus enabling intercalation electrode materials with high electrochemical performance.[19] By combining high electrical conductivity of carbon with the high redox activity of a transition metal oxide and controllably assembling the individual layers into stacked 2D heterostructures, properties can be synergistically enhanced. Three scalable approaches enabling the assembly of dissimilar layers with controlled sequence over the thickness of the heterostructure are shown to be efficient and lead to improved energy storage capabilities when such materials are used as electrodes in intercalation batteries.[18−28]

The first approach, a top-down heterostructure fabrication, consists of the exfoliation of two (or more) layered materials into single layers followed by a lamellar assembly often supported by surface functionalization to control the sequence of the layers. Advances in charge storage performance were reported even in cases when surface charges were not modified.[20,21] However, given that oxides, carbides, chalcogenides, and reduced graphene oxide (rGO) are all negatively charged, achieving a homogeneous and uniform heterostructure sequence is challenging. A strategy in which the surface of one of the materials comprising the heterostructure is positively charged via functionalization was shown to be efficient for controlling the sequence of assembling layers through electrostatic interactions, although the electrical conductivity decreased due to incorporation of functional groups.[22−24]

The second approach involves bottom-up growth of heterostructures from a solution. The atomic-scale homogeneity in solution enables lamellar self-assembly of layers induced by electrostatic interactions and often requires postassembly processing to initiate transformations leading to the formation of a 2D heterostructure. An example in which this approach has been realized shows construction of MoS_2/carbon hierarchical tubular heterostructures. Four precursor materials—Sb_2S_3 microrods, $Na_2MoO_4 \cdot 2H_2O$, thiourea (N_2H_4CS), and glucose $(C_6H_{12}O_6)$—were hydrothermally treated at 200 °C, and the obtained product was annealed at 700 °C in an $Ar(95\%)/H_2(5\%)$ mixture to remove unreacted Sb_2S_3.[25] This process produced MoS_2/carbon heterostructure electrodes that exhibited high reversible specific capacity, good rate performance, and excellent cycling stability in Na-ion batteries. Building 2D heterostructures via bottom-up processes enables unprecedented control of chemical composition and lamellar assembly; however, finding synthesis conditions, e.g., temperature, solvent, pH, etc., leading to the formation of layers of two individual materials simultaneously is challenging. Therefore, at the moment, this is the least widely used method for building 2D heterostructures, and to the best of our knowledge, there is only one example discussed above that presents a successful realization of the bottom-up approach.

The third approach combines top-down and bottom-up routes: layers of one material are prepared in the form of a single flake suspension using a chemical exfoliation approach, and the layers of the second material are grown on the surface of the flakes from the solution or formed through a chemical transformation often induced by annealing.[26−28] An elegant approach based on self-assembly of positively charged organic molecules between the layers of the negatively charged 2D transition metal compound, obtained via a top-down liquid exfoliation process followed by annealing and resulting in carbonization of the organic molecules, was successfully realized to form MoS_2/N-doped graphene (NDG) heterostructures.[28] A suspension of MoS_2 nanoflakes was produced via lithium ion intercalation in butyllithium followed by exfoliation in water. An excess amount of dopamine hydrochloride (DOPA-HCl) was then added to the suspension, leading to the formation of black flake-like floccules. This black product was freeze-dried and annealed at 600 °C under flowing Ar, producing the MoS_2/NDG heterostructure. When studied as a LIB anode, the obtained MoS_2/NDG heterostructure showed high specific capacity, excellent rate capability, and cycling stability.[28] In all the examples discussed above, the high electrochemical performance of 2D heterostructures was attributed to the formation of the intimate heterointerface between the layers of two individual materials combined together in a stacked architecture. This stable heterointerface is believed to play a key role in achieving high and stable performance by providing fast electron and ion transport.[18]

Other synthetic strategies involving chemical transformations of DOPA molecules have been shown to produce highly performing electrode materials in energy storage devices.[29,30] Polydopamine-derived materials obtained via controllable oxidation of DOPA molecules exhibited superior electrochemical performance as anodes in Li-ion and Na-ion batteries.[29] The strong adhesion property of DOPA enabled by the presence of a catechol functional group and a terminal amino group was successfully utilized to create nitrogen-doped carbon coating on the surface of $Na_3V_2(PO_4)_2F_3$ cathode material for Na-ion batteries, leading to the enhanced electrochemical performance attributed to the improved electronic conductivity.[30] Additionally, it was found that nitrogen doping of the carbon coating layer, arising from the presence of N atoms in the structure of DOPA molecules, can produce additional active sites resulting in increased specific capacity.[30] Therefore, because of the chemical composition and controllable transformations of DOPA, incorporation of this biodegradable molecule into the synthesis of electrode
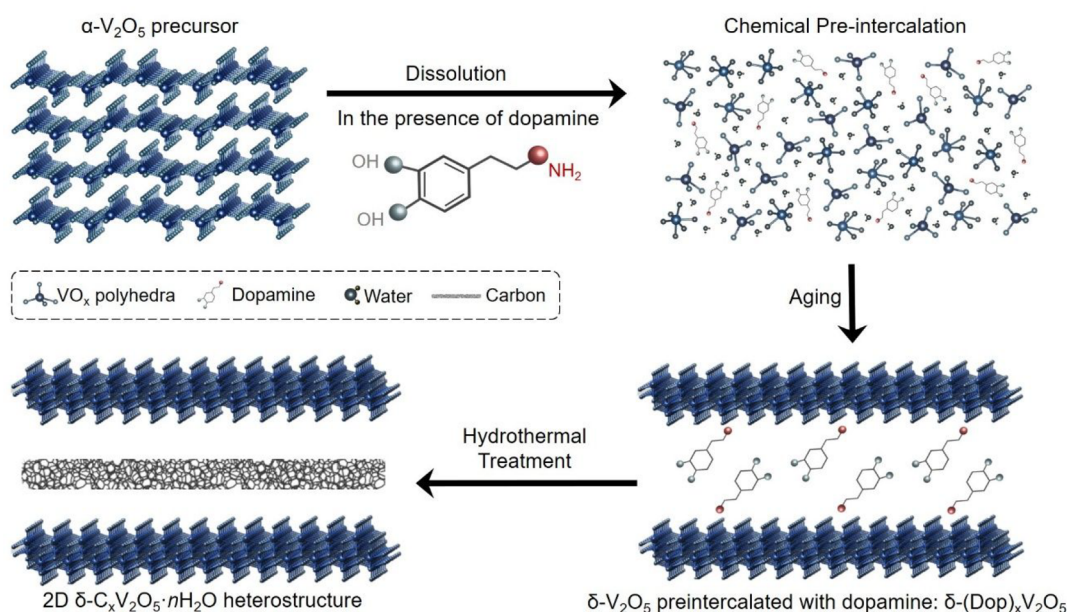
Figure 1. Schematic illustration of chemical preintercalation synthesis approach followed by hydrothermal treatment for the formation of 2D δ-$C_xV_2O_5 \cdot nH_2O$ heterostructures. Samples synthesized via the decomposition of a vanadium oxide (α-V_2O_5) precursor, which is then allowed to reconstruct into stacked bilayer chains with dopamine molecules trapped within interlayer region, forming a dopamine-preintercalated, δ-$(Dop)_xV_2O_5$, phase. Carbonization of dopamine molecules through hydrothermal treatment results in the formation of a carbon layer within interlayer region, creating a 2D δ-$C_xV_2O_5 \cdot nH_2O$ heterostructure material.

materials proved to be an efficient strategy to tune and advance electrochemical energy storage systems.

The most reliable method with the highest degree of control is the bottom-up approach, in which 2D heterostructures can be fabricated by growing a redox-active material, such as an oxide, from the solution in the presence of organic molecules followed by pyrolysis. If the lamellar assembly of the oxide layers and trapping of organic molecules between the layers can be achieved, the resulting heterostructure will be built by alternating single layers of oxide and carbon components with perfect order. To date, such materials have not been realized.

Incorporation of organic molecules between the layers of an oxide material growing from solution can be achieved via a low-cost, scalable, chemical preintercalation synthesis approach. This synthesis technique was first developed for chemical insertion of inorganic ions into the interlayer region of bilayered vanadium oxide.[4−8] It was shown that the interlayer spacing increased with an increase of the hydrated ion radius and varied between 9.62 and 13.40 Å for δ-$M_xV_2O_5$ (M = Li, Na, K, Mg, Ca). The specific capacity, cyclability, and rate performance of δ-$M_xV_2O_5$ electrodes in LIBs improved with increasing interlayer spacing.[6] Chemical preintercalation of organic molecules in the interlayer region of the bilayered vanadium oxide was shown to be possible for water-soluble molecules containing positively charged groups, allowing expansion of the interlayer spacing up to 31 Å.[9] Annealing of such hybrid organic/δ-V_2O_5 phases could potentially lead to the formation of 2D carbon/δ-V_2O_5 heterostructures. However, carbonization of organic molecules occurs at relatively high temperatures above 400 °C, and metastable layered oxides with expanded interlayer spacings, such as bilayered vanadium oxide, are not stable at such high temperatures and undergo phase transformation with the formation of atomically denser structures.[31] Therefore, utilizing a bottom-up approach for oxides is challenging.

In this article, we show that carbonization of dopamine inserted into the interlayer region of the bilayered vanadium oxide through a chemical preintercalation synthesis approach can be achieved in the course of a hydrothermal treatment process at a relatively low temperature of 220 °C without phase transformation. The synthesis approach is schematically illustrated in Figure 1. Formation of the carbon layer is confirmed through powder X-ray diffraction (XRD) analysis, Raman spectroscopy, and scanning transmission electron microscopy (STEM). The layered δ-$C_xV_2O_5 \cdot nH_2O$ material with vanadium oxide/carbon heterointerface, called here a 2D heterostructure, showed high energy storage performance, with capacities above 200 mAh g^{-1} and capacity retentions of 94% in Li-ion cells. Moreover, this heterostructured phase displays improved rate performance, with a 66% increase in capacity retention when the current was increased from 20 to 300 mA g^{-1} compared to the δ-$V_2O_5 \cdot nH_2O$ reference. Improved rate capability and cyclability of 2D δ-$V_2O_5 \cdot nH_2O$ heterostructure, as compared to the reference δ-$V_2O_5 \cdot nH_2O$ electrodes, are attributed to the increased electronic conductivity confirmed by electrochemical impedance spectroscopy (EIS) and four-probe conductivity measurements and better structural stability revealed by X-ray photoelectron spectroscopy (XPS) characterization demonstrating reduction of vanadium most likely due to the interactions between vanadium oxide and carbon layer forming in the interlayer region.

■ EXPERIMENTAL METHODS

Materials Synthesis. In a typical synthesis, dopamine hydrochloride ($(HO)_2C_6H_3CH_2CH_2NH_2 \cdot HCl$) was dispersed in 15 mL of deionized water. Then, 0.5 g of α-V_2O_5 was slowly added over a span of 5 min. A precursor dopamine:V_2O_5 molar ratio of 1:5 was used. Following, 8 mL of 30 wt % $H_2O_2(aq)$ was added dropwise over the span of 4 h. Peroxide was added slowly as the limiting reagent in the solution in an attempt to prevent oxidative polymerization of the dopamine molecules, which has been previously demonstrated.[32,33]
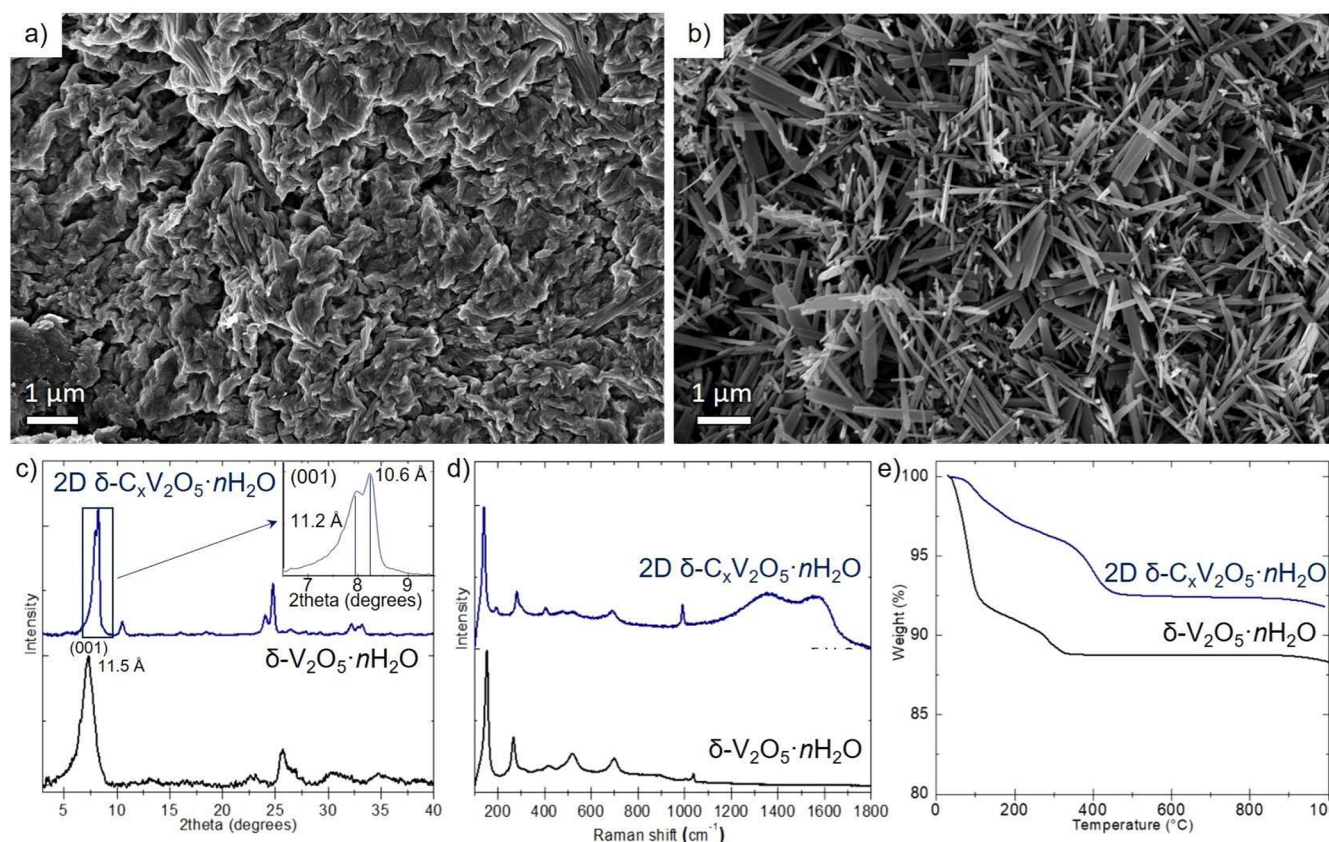
Figure 2. Morphology, structure, and chemical composition characterization of the synthesized materials. (a, b) SEM images of (a) pure δ-V$_2$O$_5$·nH$_2$O reference and (b) 2D δ-C$_x$V$_2$O$_5$·nH$_2$O heterostructure. (c) XRD patterns of both materials from 3° to 40° 2θ. (d) Raman spectra of both materials from 100 to 1800 cm^{-1}. (e) TGA weight loss curves from 25 to 1000 °C.

For the first 2 h of peroxide addition, the solution was vigorously stirred at room temperature. Then, the temperature was raised for the following 2 h to 60 °C with continued peroxide addition. After all the H$_2$O$_2$ was added, the solution was left to stir at 60 °C for 2 h. Following synthesis, samples were covered and placed in a vented fume hood and allowed to age for 4 days, which resulted in the formation of a dark brown sol. For carbonization, the resulting sols were hydrothermally treated in water in Teflon-lined autoclaves for 24 h at 220 °C. The final δ-C$_x$V$_2$O$_5$·nH$_2$O samples were filtered with copious amounts of water and dried at 100 °C under air and vacuum. Non-preintercalated δ-V$_2$O$_5$·nH$_2$O samples were also synthesized via a similar route, but without the addition of dopamine hydrochloride and no hydrothermal treatment. A pure carbon sample was synthesized by using the same approach described above, but with no α-V$_2$O$_5$ added into the synthesis. As such, dopamine alone reacts with hydrogen peroxide, forming polydopamine spheres, which are then carbonized via hydrothermal treatment.

Materials Characterization. XRD patterns were obtained using a Rigaku SmartLab X-ray diffractometer (Japan) with Cu Kα radiation. XRD patterns were acquired over a 2θ range from 5° to 40° with a step size of 0.02°. Bragg's law was used to calculate the interlayer spacing for each material from the position of the (001) peak. A Zeiss Supra 50VP (Germany) scanning electron microscope (SEM) was used to characterize material morphology. The SEM is equipped with an energy-dispersive X-ray spectrometer (EDS), which was used to analyze the material elemental composition. Thermogravimetric analysis (TGA) was performed by using a TA Instruments Q50 (TA Instruments, USA) and was conducted from room temperature to 1000 °C in air. Further crystallographic information was gathered via Raman spectroscopy. Raman spectra were obtained from 100 to 1800 cm^{-1} using a Renishaw inVia Raman microscope (Renishaw, United Kingdom) with red 633 nm light source. Diamond-knife

ultramicrotomy was used to prepare samples for high-resolution STEM imaging, which was performed at an accelerating voltage of 200 kV with an aberration-corrected JEOL JEM-2200FS TEM/STEM (JEOL USA, Peabody, MA). X-ray photoelectron spectroscopy (XPS) measurements were recorded using a Physical Electronics VersaProbe 5000 spectrometer equipped with a monochromatic Al Kα source and charge compensation. The high-resolution XPS data of the V 2p$_{3/2}$ core level binding energy region were obtained at a pass energy of 23.5 eV with a step size of 0.05 eV. Peak fitting and data analysis were performed using CasaXPS software. Electronic conductivity was determined by measuring resistivity of the pressed pellets using a Jandel Engineering Ltd. ResTest four-point probe (Jandel Engineering, United Kingdom) with a 1 mm probe distance. All pellets were pressed by using a Carver press (Carver Inc., USA) at ~80 MPa, and wafer resistivity was measured at currents between 1 and 10 μA. The reported conductivity was determined via the following equation:

$$\text{electronic conductivity (S cm}^{-1}) = \frac{1}{4.532\frac{V}{I}t}$$

where V is the measured voltage, I is the applied current, and t is the thickness of the pellets.

Electrochemical Testing. Electrodes were fabricated by mixing a slurry of 70 wt % active material, 20 wt % carbon black conductive additive, and 10 wt % poly(vinylidene fluoride) (PVDF) as a polymer binder in 1-methyl-2-pyrrolidinone (NMP). Slurries were prepared using a FlackTek Speedmixer (FlackTek Inc., SC) and cast using a doctor blade onto an Al foil current collector. 12 mm electrodes were punched from the film and were then dried at 100 °C for 12 h in a vacuum oven before being transferred into an Ar-filled glovebox.

All electrodes were cycled in a Li-ion system using 2032 coin cells. The following components were used to assemble the cell: Li metal foil (Alfa Aesar) as the counter/reference electrode, Celgard as the
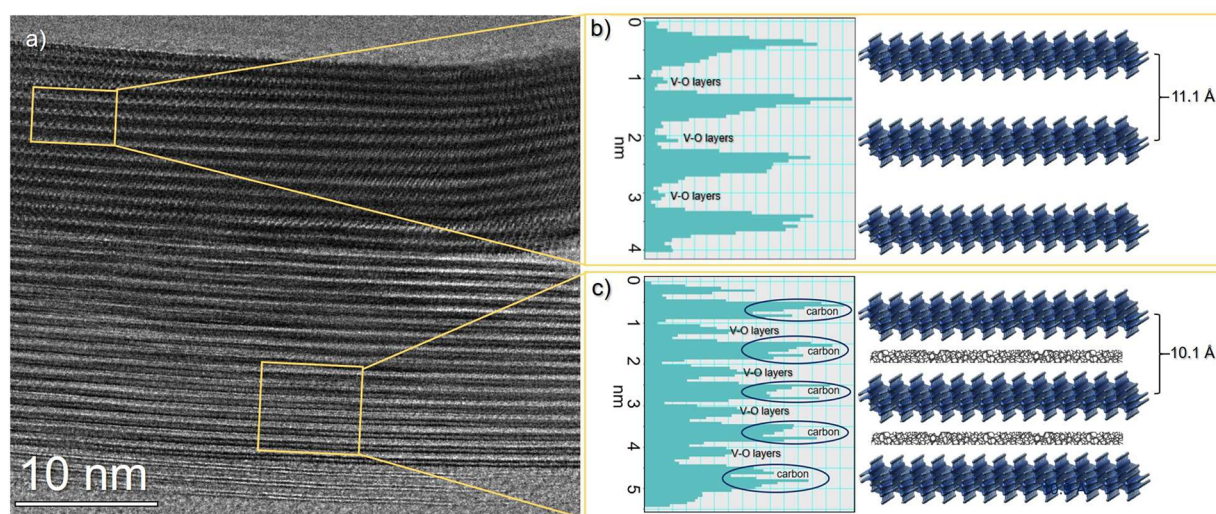
Figure 3. Microscopy characterization of 2D δ-$C_xV_2O_5 \cdot nH_2O$ heterostructure: (a) BF-STEM image of a 2D δ-$V_2O_5 \cdot nH_2O$ nanobelt (top) and 2D δ-$C_xV_2O_5 \cdot nH_2O$ nanobelt (bottom). (b, c) Averaged line histograms (left) extracted by analyzing contrast in rectangular areas outlined in yellow in (a); dips in intensity (circled in dark blue in (c)) are attributed to carbon layers in the interlayer region of δ-V_2O_5. Schematic illustrations shown on the right in (b) and (c) correspond to the formed δ-$V_2O_5 \cdot nH_2O$ (top) and 2D δ-$C_xV_2O_5 \cdot nH_2O$ heterostructure (bottom) regions.

separator, and 1 M $LiPF_6$ in EC:DEC (BASF LP40) as the electrolyte. Cyclic voltammetry (CV) and electrochemical impedance spectroscopy (EIS) characterization was performed using a Biologic VMP3 multichannel potentiostat/galvanostat. CV curves were obtained by cycling electrodes in the 2.0−4.0 V voltage window with a scan rate of 0.1 mV s^{-1}. EIS measurements were performed by applying an alternating voltage (10 mV) in the frequency range between 10 mHz and 200 kHz at the open circuit voltage. Galvanostatic cycling experiments were conducted at a current density of 20 mA g^{-1} in an Arbin battery testing station (Arbin Instruments, USA). The rate capability of the synthesized materials was investigated at increasing current densities (20, 30, 60, 300, and 20 mA g^{-1} for 10 cycles at each current density).

RESULTS AND DISCUSSION

Figure 1 illustrates the bottom-up synthesis approach used to form a 2D δ-$C_xV_2O_5 \cdot nH_2O$ heterostructure. Using chemical preintercalation of water-soluble, positively charged dopamine molecules, a δ-$(Dop)_xV_2O_5$ layered structure was obtained as a precipitate in a course of the sol−gel process followed by extended aging. Hydrothermal treatment of the δ-$(Dop)_xV_2O_5$ precipitate induced carbonization of the dopamine confined between the V−O layers. This synthetic strategy leads to the formation of a material with the crystal structure built from V−O bilayers and carbon layers incorporated in between. The produced material represents the first example of a 2D oxide/carbon heterointerface with precisely controlled alternating sequence of single oxide/single carbon layers enabled by atomic-scale homogeneity and electrostatic interaction of oxide and carbon precursors in solution offered by chemical preintercalation. The regions with precisely controlled sequence of oxide and carbon layers, confirmed by detailed XRD, Raman spectroscopy, TGA, and STEM characterization (Figures 2 and 3), make this material uniquely different from the vanadium oxide−carbon composites reported previously.[34,35]

Figures 2a and 2b show SEM images of the bilayered δ-$V_2O_5 \cdot nH_2O$ reference material (Figure 2a) and the synthesized 2D δ-$C_xV_2O_5 \cdot nH_2O$ heterostructure (Figure 2b). These two materials have significantly different morphologies. The δ-

$V_2O_5 \cdot nH_2O$ reference material consisted of buckled sheets with one-dimensional particles starting to form. On the other hand, the SEM image of the 2D δ-$C_xV_2O_5 \cdot nH_2O$ heterostructure exhibited one-dimensional nanoparticles, with widths of 100−200 nm and lengths between 1 and 3 μm (Figure 2b). δ-$C_xV_2O_5 \cdot nH_2O$ nanoparticles are formed after hydrothermal treatment of the dopamine-preintercalated bilayered vanadium oxide, and the shape of the particles is governed by the high pressure and temperature that lead to the oriented growth of nanostructures. The δ-$V_2O_5 \cdot nH_2O$ reference material, on the other hand, was prepared without hydrothermal treatment and at lower temperatures not exceeding 100 °C used for dehydration, thus resulting in a material with morphology different from that exhibited by the 2D δ-$C_xV_2O_5 \cdot nH_2O$ heterostructure.

Figure 2c shows the XRD patterns of both δ-$V_2O_5 \cdot nH_2O$ and 2D δ-$C_xV_2O_5 \cdot nH_2O$ heterostructure materials. The XRD pattern of the synthesized δ-$V_2O_5 \cdot nH_2O$ reference sample is in good agreement with data in the literature,[11,12,15−17,36] corresponding to a layered structure with an interlayer spacing of 11.5 Å calculated from the position of the (001) reflection in the XRD pattern, which occurs at ∼7.6° 2θ. There is an additional (003) reflection visible in the XRD pattern at 26° 2θ. The 2D δ-$C_xV_2O_5 \cdot nH_2O$ heterostructure showed an XRD pattern that is similar to the δ-$V_2O_5 \cdot nH_2O$ reference material, though with some notable differences. First, the (001) reflection in the XRD pattern appears as two overlapping peaks with positions at 7.9° and 8.3° 2θ corresponding to 11.2 and 10.6 Å interlayer spacings, respectively. This peak splitting is more apparent at higher 2θ angles where two visible (003) peaks are observed at ∼23° and ∼24° 2θ. We will show via STEM analysis that these two separate XRD patterns correspond to (1) stacked layers of pure bilayered δ-$V_2O_5 \cdot nH_2O$ with no carbon present in the interlayer region and (2) stacked V−O layers with an additional layer present in between. Raman spectroscopy measurements suggest that the formed layer is a carbon layer due to the presence of carbon D and G bands in the Raman spectra of the 2D δ-$C_xV_2O_5 \cdot nH_2O$ heterostructure (Figure 2d). The δ-$V_2O_5 \cdot nH_2O$ reference

material was synthesized via chemical preintercalation and extended aging without using a hydrothermal treatment. It was determined that hydrothermal treatment of this reference sample leads to a phase change from the δ-V_2O_5 phase to the α-V_2O_5 phase (Figure S1, Supporting Information). This is a further indication that the δ-V_2O_5 reference material and the 2D δ-$C_xV_2O_5 \cdot nH_2O$ heterostructure are distinctly different, as hydrothermal treatment of the δ-$(Dop)_xV_2O_5$ precursor did not lead to a phase change of the bilayered structure.

Raman spectra of both the pristine δ-$V_2O_5 \cdot nH_2O$ and the 2D δ-$C_xV_2O_5 \cdot nH_2O$ heterostructure, shown in Figure 2d, also confirm the formation of V–O bilayers.[16,31] Bands occurring at or below 1050 cm^{-1} are assigned to vibration modes of δ-V_2O_5 in both samples. The most prominent bands occurring at 150 and 141 cm^{-1} in the Raman spectra of δ-$V_2O_5 \cdot nH_2O$ and 2D δ-$C_xV_2O_5 \cdot nH_2O$ heterostructure, respectively, are assigned to the skeleton vibration of layered-type δ-V_2O_5. An O–V–O bending vibration mode is found in both samples at 266 and 281 cm^{-1} (for δ-V_2O_5 and 2D δ-V_2O_5/NDG materials, respectively) and a V–O bond stretching band at 413 and 409 cm^{-1} (δ-$V_2O_5 \cdot nH_2O$ and 2D δ-$C_xV_2O_5 \cdot nH_2O$ materials, respectively).[16,31] A vanadyl V=O stretching vibration occurs at 1037 cm^{-1} for the δ-$V_2O_5 \cdot nH_2O$ material and 991 cm^{-1} for the 2D δ-$C_xV_2O_5 \cdot nH_2O$ heterostructure. There are two bands corresponding to the V–O–V symmetric stretching at 518 and 695 cm^{-1}, which are also present in both samples.[16,31] Analysis of the Raman spectra confirms that the overall bonding character of the δ-V_2O_5 structure is similar in both materials; however, they exhibit distinct differences, implying that these materials are different.

There are no bands above 1050 cm^{-1} present in the Raman spectrum of δ-$V_2O_5 \cdot nH_2O$ sample, while the Raman spectrum of the 2D δ-$C_xV_2O_5 \cdot nH_2O$ heterostructure shows two broad bands at ∼1329 and 1560 cm^{-1} (Figure 2d), which can be assigned to the characteristic D and G bands of carbon.[28,37] A D:G intensity ratio of 1.01 in the Raman spectrum of the 2D δ-$C_xV_2O_5 \cdot nH_2O$ heterostructure suggests that the carbon layer is highly defect-rich and most likely corresponds to the amorphous carbon structure. To understand the structure of carbon, 2D heterostructure particles containing higher concentration of carbon need to be analyzed. We are currently working on modifying the synthesis approach with the goal to increase carbon content. The presence of these bands in the Raman spectrum of the heterostructure is in agreement with XRD data, suggesting the formation of a carbon layer within the structure of the bilayered phase. It should be noted that both the XRD pattern and Raman spectrum of the 2D δ-$C_xV_2O_5 \cdot nH_2O$ sample show no peaks or modes that correspond to dopamine hydrochloride (Figure S2), indicating complete transformation of the organic precursor into carbon.

Figure 2e shows the TGA weight loss curves for both δ-$V_2O_5 \cdot nH_2O$ reference material and 2D δ-$C_xV_2O_5 \cdot nH_2O$ heterostructure from 25 to 1000 °C in air. The δ-$V_2O_5 \cdot nH_2O$ reference material shows three weight loss regions, from 0–100 °C, 100–270 °C, and 270–400 °C, after which the weight remains constant. The first weight loss region corresponds to the evaporation of physisorbed water, while the latter two regions correspond to the loss of structural, crystallographically bound water molecules, which reside in the interlayer spacing of δ-$V_2O_5 \cdot nH_2O$.[15,36] The water content in the δ-$V_2O_5 \cdot nH_2O$ reference material was determined to be 0.5 molecules of water, corresponding to the chemical formula of δ-$V_2O_5 \cdot 0.5H_2O$. According to our study of the thermal stability

of bilayered vanadium oxides, the region of 100–510 °C should be used for the evaluation of the hydration degree.[31] For the 2D δ-$C_xV_2O_5 \cdot nH_2O$ heterostructure, the thermally induced weight loss behavior shows different features compared to the δ-$V_2O_5 \cdot nH_2O$ reference material (Figure 2e). To better understand the chemical composition of the 2D δ-$C_xV_2O_5 \cdot nH_2O$ heterostructure, pure carbon was synthesized using the same hydrothermal treatment conditions with dissolved dopamine precursor without the addition of any vanadium oxide precursor. Figure S3 shows the TGA weight loss curve obtained for the pure carbon particles as compared to the δ-$V_2O_5 \cdot nH_2O$ reference material and the 2D δ-$C_xV_2O_5 \cdot nH_2O$ heterostructure. The TGA weight loss curve of pure carbon has several regions of weight loss over the temperature range 25–600 °C. Pure carbon exhibited significant weight loss between 450 and 600 °C, a region in which no weight loss occurs for the 2D δ-$C_xV_2O_5 \cdot nH_2O$ heterostructure. Therefore, it can be concluded that the 2D δ-$C_xV_2O_5 \cdot nH_2O$ heterostructure does not contain any significant amount of pure carbon particles separate from the bilayered structure, which was achieved by thorough washing of the precipitates formed in the sol–gel step of the synthesis process leading to the removal of unreacted dopamine molecules. In addition, the absence of pure carbon particles is supported by the SEM imaging of the 2D δ-$C_xV_2O_5 \cdot nH_2O$ heterostructure (Figure 2b) and the pure carbon material (Figure S4) showing distinctly different morphology. The presence of both water molecules and carbon in the interlayer region of the 2D δ-$C_xV_2O_5 \cdot nH_2O$ heterostructure in relatively small amounts makes the analysis of the chemical composition of this material challenging. Better understanding of the roles of individual components in the heterostructure requires synthetic tunability of carbon:V_2O_5 and H_2O:V_2O_5 ratios (the values of "x" and "n" in the δ-$C_xV_2O_5 \cdot nH_2O$ formula), which is the focus of our current research.

Figure 3 shows a bright-field (BF) STEM image of the 2D δ-$C_xV_2O_5 \cdot nH_2O$ heterostructure particle consisting of two nanobelts. The horizontal light gray stripes correspond to the V–O layers, and by measuring the distance between them, a (001) lattice spacing can be determined. In the upper nanobelt, the interlayer spacing (dark gray regions correspond to the interlayer region) is measured to be 11.1 Å, in excellent agreement with the first peak of the split (001) reflection observed in the XRD patterns of heterostructure in Figure 2c, which we assign to bilayered δ-$V_2O_5 \cdot nH_2O$ with no carbon layer. In the lower nanobelt, an interlayer spacing of 10.1 Å was determined by measuring distance between the light gray stripes. This distance is close to the interlayer spacing calculated from the second peak of the split (001) reflection in the XRD pattern of the 2D δ-$C_xV_2O_5 \cdot nH_2O$ heterostructure (Figure 2c), assigned to the bilayered vanadium oxide structure containing a carbon layer between two V–O layers. Within this lower nanobelt a line of light gray color is observed in the middle of the interlayer regions, which suggests the presence of a carbon layer. These features are further highlighted in the line-averaged histogram extracted from the regions highlighted in yellow and presented in Figure 3b (upper nanobelt) and Figure 3c (lower nanopbelt). For the upper nanobelt (Figure 3b), the line-averaged histogram shows only deep dips in contrast intensity, which correspond to the V–O layers. In the histogram of the lower nanobelt (Figure 3c), the V–O bilayers are marked by the deepest dips in intensity, while the additional dips in the dark, high-intensity interlayer regions,

circled in dark blue, provide direct evidence for the presence of carbon layers. The deviation between 10.1 and 10.6 Å, measured via STEM imaging and XRD pattern analysis, respectively, may be due to the local nature vs bulk nature of the two characterization methods. This sensitivity of the nanobelts to electron radiolysis made local spectroscopic measurements by techniques such as electron energy loss spectroscopy impossible due to the higher required electron dose, and it was thus not possible to determine the intermittency of the carbon layers within the interlayer region of the bilayered vanadium oxide structure.

Formation of the carbon layer between the V−O layers was further verified via electronic conductivity measurements performed using a four-point probe technique on pressed pellets of both the δ-$V_2O_5 \cdot nH_2O$ reference material and the 2D δ-$C_xV_2O_5 \cdot nH_2O$ heterostructure (Table 1). The electronic

Table 1. Electronic Conductivity Determined by Using a Four-Probe Technique on Pressed Pellets

	electronic conductivity (S cm^{-1})
δ-$V_2O_5 \cdot nH_2O$	1×10^{-5}
2D δ-$C_xV_2O_5 \cdot nH_2O$	1×10^{-3}

conductivity of the 2D δ-$C_xV_2O_5 \cdot nH_2O$ heterostructure phase (10^{-3} S cm^{-1}) is 2 orders of magnitude higher than that of the δ-$V_2O_5 \cdot nH_2O$ reference material (10^{-5} S cm^{-1}). Electrochemical impedance spectroscopy (EIS) measurements (Figure S5) revealed that the diameter of the semicircles at the high-to-middle frequencies of the cell containing δ-$C_xV_2O_5 \cdot nH_2O$ heterostructure electrode is smaller than that of a cell containing δ-$V_2O_5 \cdot nH_2O$ reference electrode, which is attributed to the improved electron transport capability of active material and in good agreement with the four-probe conductivity measurements. This significant improvement of electronic conductivity further supports the STEM observations, showing localized formation of the carbon layers. On the basis of our combined XRD, Raman spectroscopy, TGA, STEM, EIS, and electronic conductivity measurements analyses, we believe that carbon layers are created via carbonization of the chemically preintercalated dopamine molecules and intermittently form between V−O layers.

Electrochemical performance of the δ-$V_2O_5 \cdot nH_2O$ reference and the 2D δ-$C_xV_2O_5 \cdot nH_2O$ heterostructure electrodes in Li-ion nonaqueous half-cells is summarized in Table 2 and discussed in detail below. Figure 4 shows cycling results of the cells containing δ-$V_2O_5 \cdot nH_2O$ and δ-$C_xV_2O_5 \cdot nH_2O$ electrodes. The cyclic voltammetry (CV) curves of the Li-ion cell containing δ-$C_xV_2O_5 \cdot nH_2O$ heterostructure electrode (Figure S6) demonstrate three reversible redox peaks indicative of typical ion insertion type behavior. The peaks appear at

Table 2. Electrochemical Performance of the δ-$V_2O_5 \cdot nH_2O$ Reference and 2D δ-$C_xV_2O_5 \cdot nH_2O$ Heterostructure Electrodes in Li-Ion Cells

material	initial discharge capacity at 20 mA g^{-1} (mAh g^{-1})	capacity retention after 30 cycles at 20 mA g^{-1} (%)	capacity retention at 300 mA g^{-1} (%)
δ-$V_2O_5 \cdot nH_2O$	219	58	10
2D δ-$C_xV_2O_5 \cdot nH_2O$	206	94	75

approximately the same voltages as the plateaus in galvanostatic discharge−charge curves (Figure 4b). However, the single unresolved plateau at ∼2.5 V vs Li/Li$^+$ in discharge/charge curve (Figure 4b) appears as a pair of closely located peaks in CV curve (Figure S6), indicating two sites for Li$^+$ ion intercalation. At a current density of 20 mA g^{-1}, δ-$V_2O_5 \cdot nH_2O$ electrodes showed an initial discharge capacity of 219 mAh g^{-1}, which quickly decayed over extended cycling, exhibiting a capacity retention of 58% after 30 discharge/charge cycles. While the 2D δ-$C_xV_2O_5 \cdot nH_2O$ electrodes demonstrated a slightly lower initial discharge capacity of 206 mAh g^{-1}, notably they demonstrated significantly higher capacity retention compared to the reference δ-$V_2O_5 \cdot nH_2O$ material, with 94% of the initial capacity retained after 30 cycles (Figure 4c,d). To the best of our knowledge, this is the highest capacity retention ever demonstrated by bilayered vanadium oxide electrodes, synthesized via sol-gel based processes, in Li-ion cells.[6,11,13] The high capacity retention is attributed to the formation of the robust heterointerface between the carbon and V−O layers, which stabilizes the lamellar ordering of the layers and leads to improved structural and therefore electrochemical stability. A similar structure strengthening effect has been reported for polyaniline (PANI)-reinforced manganese oxide layers that exhibited high electrochemical stability in aqueous zinc-ion batteries.[38] Partial reduction of the intralayer vanadium ions in 2D δ-$C_xV_2O_5 \cdot nH_2O$ heterostructure, revealed by XPS measurements (Figure S8 and Table S1), confirms formation of additional bonds, which could arise from interaction between vanadium oxide bilayers with islands of carbon forming in the interlayer region via dopamine carbonization during hydrothermal treatment. The carbon-reinforced structure of bilayered vanadium oxide exhibits better structural and therefore electrochemical stability as compared to the reference δ-$C_xV_2O_5 \cdot nH_2O$ electrodes. Because of the rapid capacity fading of δ-$V_2O_5 \cdot nH_2O$ electrodes, several tens of intercalation/deintercalation cycles are usually used to demonstrate that certain approaches can lead to superior cyclability. The extended cycling of 2D δ-$C_xV_2O_5 \cdot nH_2O$ electrodes revealed that 61% of initial capacity remains after 100 cycles (Figure S7). Further improvement in capacity retention can be achieved by increasing the fraction of interlayer carbon in the structure of bilayered vanadium oxide electrodes.

The rate capability evaluated by cycling Li-ion cells containing the δ-$V_2O_5 \cdot nH_2O$ reference and the 2D δ-$C_xV_2O_5 \cdot nH_2O$ heterostructure electrodes at various current densities (Figure 4e,f) clearly shows that the electrode material containing carbon layers exhibits significantly higher capacities at increased current densities. The 2D δ-$C_xV_2O_5 \cdot nH_2O$ heterostructure electrode demonstrated a capacity of ∼155 mAh g^{-1} at a current density of 300 mA g^{-1}, which corresponds to 75% of the capacity delivered by this material at a current density of 20 mA g^{-1} (206 mAh g^{-1}). This capacity retention is substantially higher than that exhibited by the δ-$V_2O_5 \cdot nH_2O$ reference electrodes, which demonstrated only 10% capacity retention when the current density was changed from 20 to 300 mA g^{-1} (Figure 4e,f). When the current density was brought back to the low value of 20 mA g^{-1}, the specific capacity of the 2D δ-$C_xV_2O_5 \cdot nH_2O$ heterostructure electrode showed a specific capacity of 200 mAh g^{-1}, similar to the capacity initially exhibited at 20 mA g^{-1}. At the same time, the specific capacity of the δ-$V_2O_5 \cdot nH_2O$ reference electrode at 20 mA g^{-1} returned to a capacity of 141 mAh g^{-1} after being

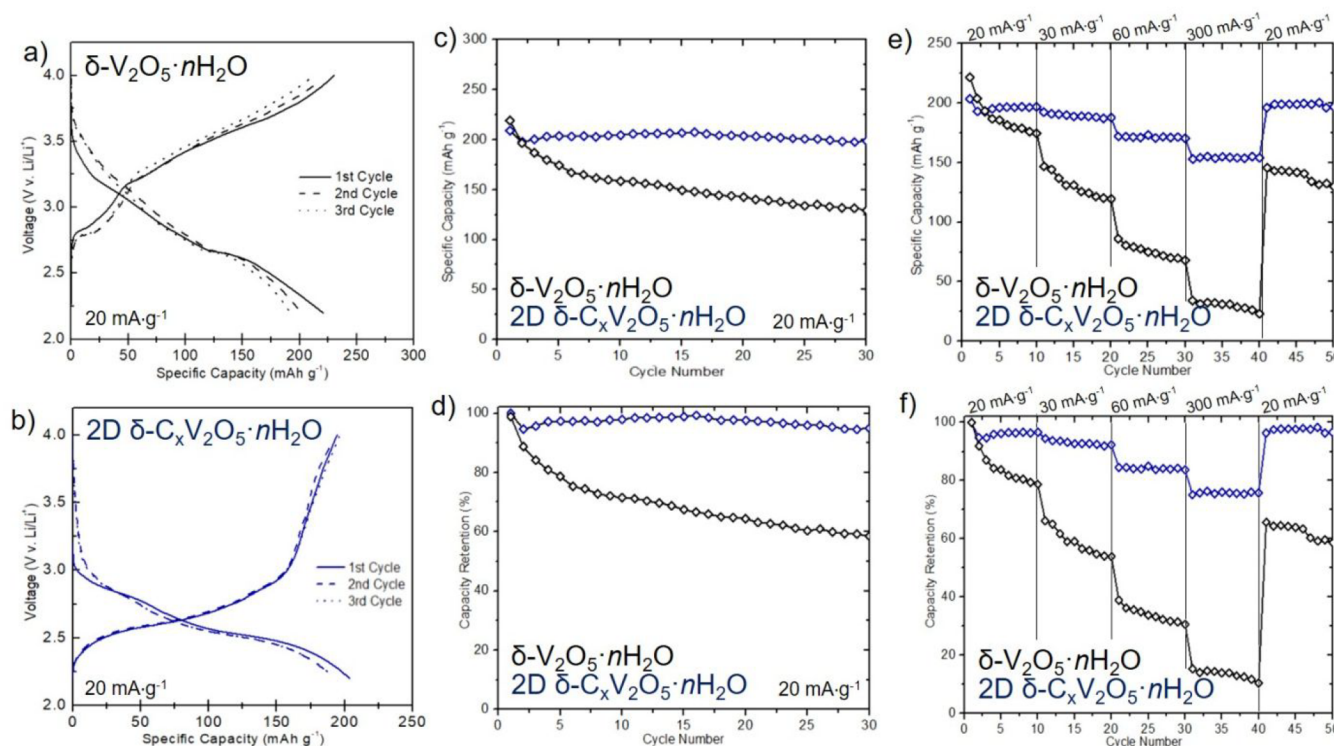**Figure 4.** Electrochemical characterization of δ-$V_2O_5 \cdot nH_2O$ reference and 2D δ-$C_xV_2O_5 \cdot nH_2O$ heterostructure electrodes in Li-ion cells in the voltage range of 2.2–4.0 V. (a, b) First, second, and third cycles of discharge−charge curves of Li-ion half cells containing (a) pure δ-$V_2O_5 \cdot nH_2O$ phase and (b) 2D δ-$C_xV_2O_5 \cdot nH_2O$ heterostructure, cycled at a current density of 20 mA g^{-1}. (c, d) Extended cycling of both electrodes at a current density of 20 mA g^{-1}: (c) specific capacity and (d) capacity retention calculated by normalizing by the first discharge capacity. (e, f) Rate capability performance of both electrodes (electrodes were cycled for ten cycles at increasing current densities of 20, 30, 60, and 300 mA g^{-1} and returning to 20 mA g^{-1}): (e) specific capacity and (f) capacity retention calculated by normalizing by the first discharge capacity.

cycled at higher current rates, which is 33 mAh g^{-1} lower than the capacity of the 10th cycle (174 mAh g^{-1}), i.e., the last cycle of the initial 20 mA g^{-1} step (Figure 4e,f). Such electrochemical behavior indicates improved charge transport kinetics, leading to improved tolerance toward high currents. The increase in rate capability of the heterostructure electrodes can be ascribed to the improved electron transport via the carbon layers accommodated between V−O layers combined with the presence of 2D diffusion channels available for the electrochemically cycled Li$^+$ ion movement. The presence of the carbon layer in the interlayer region of bilayered vanadium oxide is likely to affect diffusion of electrochemically cycled ions, especially in the case of defect-rich carbon with amorphous nature. In this work, however, the carbon layers formed intermittently, and carbon-free areas in the interlayer region enable efficient transport of Li$^+$ ions.

The improved electrochemical performance of the 2D δ-$C_xV_2O_5 \cdot nH_2O$ heterostructure electrode compared to the δ-$V_2O_5 \cdot nH_2O$ reference material in Li-ion cells is attributed to (1) the increased electronic conductivity of the heterostructure enabled by improved electron transport via carbon layers and (2) the intimate interface between electrochemically active oxide layers and electronically conductive carbon layers enhancing structural, and therefore electrochemical, stability. In combination, these two factors lead to substantially higher capacity retention in galvanostatic cycling and rate capability experiments. The carbon coating layer forming on the surface of particles due to the strong adhesion property of dopamine molecules[30] could further improve electronic conductivity of bilayered vanadium oxide electrodes. Additionally, the different

morphology of δ-V_2O_5 and δ-$C_xV_2O_5 \cdot nH_2O$ particles could contribute to the observed differences in electrochemical performance. Further improvements can be achieved by developing strategies within the chemical preintercalation synthesis approach that can lead to the formation of continuous carbon layers between the oxide layers and expansion of the interlayer spacing. Partial or complete removal of interlayer water, achievable via postsynthesis annealing,[31] can be also used to enhance energy storage properties of 2D heterostructure electrodes.[39]

■ CONCLUSIONS

This report is the first demonstration of a 2D oxide−carbon heterointerface created via chemical preintercalation of dopamine molecules followed by a hydrothermal treatment process. Formation of the 2D δ-$C_xV_2O_5 \cdot nH_2O$ heterostructure is confirmed by combining results from SEM, XRD, TGA, XPS, Raman spectroscopy, and STEM characterization methods. Carbon layers form intermittently between the layers of vanadium oxide. Four-probe conductivity measurements revealed a two orders of magnitude improvement in the electronic conductivity of the 2D δ-$C_xV_2O_5 \cdot nH_2O$ heterostructure over the δ-$V_2O_5 \cdot nH_2O$ reference material, in agreement with EIS measurements. The electrodes containing carbon layers exhibited substantially improved capacity retention under galvanostatic cycling conditions and increased tolerance toward high currents compared to the pure bilayered vanadium oxide electrodes. The significant improvement in capacity retention and rate performance of the 2D δ-$C_xV_2O_5 \cdot$

nH$_2$O heterostructure electrodes in Li-ion cells is attributed to the controllable formation of carbon layers between the layers of bilayered vanadium oxide, leading to improvements in electronic conductivity and structural stability of the heterostructure electrode. The chemical preintercalation synthesis approach is based on low-temperature, scalable sol−gel methods, unlike single flake, bottom-up assembly methods that have been studied previously. In addition, this approach is versatile and can be applied to other transition metal oxide electrode structures.

■ ASSOCIATED CONTENT

ⓢ Supporting Information

The Supporting Information is available free of charge at https://pubs.acs.org/doi/10.1021/acsaem.0c00274.

Photograph, SEM image, XRD pattern, and EDX spectrum of α-V$_2$O$_5$ nanowires formed via hydrothermal treatment of precipitate without chemically preintercalated species; XRD pattern and Raman spectrum of dopamine hydrochloride; TGA weight loss curves of δ-V$_2$O$_5$·nH$_2$O reference material, 2D δ-C$_x$V$_2$O$_5$·nH$_2$O heterostructure, and carbon obtained via hydrothermal treatment of dopamine; SEM image of pure dopamine-derived carbon particles; Nyquist plots of the δ-V$_2$O$_5$·nH$_2$O and δ-C$_x$V$_2$O$_5$·nH$_2$O electrodes; CV curves and extended galvanostatic cycling data of the 2D δ-C$_x$V$_2$O$_5$·nH$_2$O electrodes in Li-ion cells; XPS spectra of the δ-V$_2$O$_5$·nH$_2$O and δ-C$_x$V$_2$O$_5$·nH$_2$O materials with analysis (PDF)

■ AUTHOR INFORMATION

Corresponding Author

Ekaterina Pomerantseva − *Department of Materials Science and Engineering, Drexel University, Philadelphia, Pennsylvania 19104, United States;* ⓞ orcid.org/0000-0002-6765-7133; Phone: 215-571-4612; Email: ep423@drexel.edu; Fax: 215-895-6760

Authors

Mallory Clites − *Department of Materials Science and Engineering, Drexel University, Philadelphia, Pennsylvania 19104, United States*

Ryan Andris − *Department of Materials Science and Engineering, Drexel University, Philadelphia, Pennsylvania 19104, United States*

David A. Cullen − *Center for Nanophase Materials Sciences, Oak Ridge National Laboratory, Oak Ridge, Tennessee 37831, United States;* ⓞ orcid.org/0000-0002-2593-7866

Karren L. More − *Center for Nanophase Materials Sciences, Oak Ridge National Laboratory, Oak Ridge, Tennessee 37831, United States*

Complete contact information is available at:
https://pubs.acs.org/10.1021/acsaem.0c00274

Author Contributions

E.P. developed the concept and designed the experiments. M.C. and R.A. performed experimental work including synthesis, characterization, and electrochemical testing. D.C. and K.M. performed STEM analysis. All authors contributed to the analysis and interpretation of the obtained experimental data and writing of this manuscript.

Notes

The authors declare no competing financial interest.

■ ACKNOWLEDGMENTS

■ REFERENCES

(1) Turcheniuk, K.; Bondarev, D.; Singhal, V.; Yushin, G. Ten years left to redesign lithium-ion batteries. *Nature* 2018, *559*, 467−470.

(2) Nitta, N.; Wu, F.; Lee, J. T.; Yushin, G. Li-ion battery materials: present and future. *Mater. Today* 2015, *18* (5), 252−264.

(3) Petkov, V.; Trikalitis, P. N.; Bozin, E. S.; Billinge, S. J. L.; Vogt, T.; Kanatzidis, M. G. Structure of V$_2$O$_5$·nH$_2$O Xerogel Solved by the Atomic Pair Distribution Function Technique. *J. Am. Chem. Soc.* 2002, *124* (34), 10157−10162.

(4) Clites, M.; Hart, J. L.; Taheri, M. L.; Pomerantseva, E. Chemically Preintercalated Bilayered K$_x$V$_2$O$_5$·nH$_2$O Nanobelts as a High-Performing Cathode Material for K-Ion Batteries. *ACS Energy Letters* 2018, *3* (3), 562−567.

(5) Clites, M.; Byles, B. W.; Pomerantseva, E. Bilayered Vanadium Oxide as the Host Material for Reversible Beyond Lithium Ion Intercalation. *Adv. Mater. Lett.* 2017, *8* (6), 679−688.

(6) Clites, M.; Pomerantseva, E. Bilayered vanadium oxides by chemical pre-intercalation of alkali and alkali-earth ions as battery electrodes. *Energy Storage Materials* 2018, *11*, 30−37.

(7) Clites, M.; Byles, B. W.; Pomerantseva, E. Effect of aging and hydrothermal treatment on electrochemical performance of chemically pre-intercalated Na-V-O nanowires for Na-ion batteries. *J. Mater. Chem. A* 2016, *4* (20), 7754−7761.

(8) Clites, M.; Pomerantseva, E. *The Ion Dependent Change in the Mechanism of Charge Storage of Chemically Preintercalated Bilayered Vanadium Oxide Electrodes*; SPIE: Low Dimensional Materials and Devices, 2017; Vol. 10349, p 9.

(9) Clites, M.; Pomerantseva, E. *Synthesis of Hybrid Layered Electrode Materials via Chemical Pre-Intercalation of Linear Organic Molecules*; SPIE: Low Dimensional Materials and Devices, 2018; Vol. 10725, p 9.

(10) Lee, C.-Y.; Marschilok, A. C.; Subramanian, A.; Takeuchi, K. J.; Takeuchi, E. S. Synthesis and characterization of sodium vanadium oxide gels: the effects of water (n) and sodium (x) content on the electrochemistry of Na$_x$V$_2$O$_5$·$_n$H$_2$O. *Phys. Chem. Chem. Phys.* 2011, *13*, 18047−18054.

(11) Moretti, A.; Maroni, F.; Osada, I.; Nobili, F.; Passerini, S. V$_2$O$_5$ Aerogel as a Versatile Cathode Material for Lithium and Sodium Batteries. *ChemElectroChem.* 2015, *2* (4), 529−537.

(12) Moretti, A.; Secchiaroli, M.; Buchholz, D.; Giuli, G.; Marassi, R.; Passerini, S. Exploring the Low Voltage Behavior of V$_2$O$_5$ Aerogel as Intercalation Host for Sodium Ion Battery. *J. Electrochem. Soc.* 2015, *162* (14), A2723−A2728.

(13) Moretti, A.; Giuli, G.; Trapananti, A.; Passerini, S. Electrochemical and structural investigation of transition metal doped V$_2$O$_5$ sono-aerogel cathodes for lithium metal batteries. *Solid State Ionics* 2018, *319*, 46−52.

(14) Tepavcevic, S.; Liu, Y.; Zhou, D.; Lai, B.; Maser, J.; Zuo, X.; Chan, H.; Král, P.; Johnson, C. S.; Stamenkovic, V.; Markovic, N. M.; Rajh, T. Nanostructured Layered Cathode for Rechargeable Mg-Ion Batteries. *ACS Nano* 2015, *9* (8), 8194−8205.

(15) Tepavcevic, S.; Connell, J. G.; Lopes, P. P.; Bachhav, M.; Key, B.; Valero-Vidal, C.; Crumlin, E. J.; Stamenkovic, V. R.; Markovic, N. M. Role of structural hydroxyl groups in enhancing performance of

electrochemically-synthesized bilayer V_2O_5. *Nano Energy* **2018**, *53*, 449−457.

(16) Su, D.; Wang, G. Single-Crystalline Bilayered V_2O_5 Nanobelts for High-Capacity Sodium-Ion Batteries. *ACS Nano* **2013**, *7* (12), 11218−11226.

(17) Wei, Q.; Liu, J.; Feng, W.; Sheng, J.; Tian, X.; He, L.; An, Q.; Mai, L. Hydrated vanadium pentoxide with superior sodium storage capacity. *J. Mater. Chem. A* **2015**, *3* (15), 8070−8075.

(18) Pomerantseva, E.; Gogotsi, Y. Two-dimensional heterostructures for energy storage. *Nat. Energy* **2017**, *2*, 17089.

(19) Pomerantseva, E.; Bonaccorso, F.; Feng, X.; Cui, Y.; Gogotsi, Y. Energy storage: The future enabled by nanomaterials. *Science* **2019**, *366* (6468), eaan8285.

(20) Xu, S.; Dall'Agnese, Y.; Li, J.; Gogotsi, Y.; Han, W. Thermally Reduced Graphene/MXene Film for Enhanced Li-ion Storage. *Chem. - Eur. J.* **2018**, *24* (69), 18556−18563.

(21) Liu, W.; Wang, Z.; Su, Y.; Li, Q.; Zhao, Z.; Geng, F. Molecularly Stacking Manganese Dioxide/Titanium Carbide Sheets to Produce Highly Flexible and Conductive Film Electrodes with Improved Pseudocapacitive Performances. *Adv. Energy Mater.* **2017**, *7* (22), 1602834.

(22) Xiong, P.; Ma, R.; Sakai, N.; Nurdiwijayanto, L.; Sasaki, T. Unilamellar Metallic MoS_2/Graphene Superlattice for Efficient Sodium Storage and Hydrogen Evolution. *ACS Energy Letters* **2018**, *3* (4), 997−1005.

(23) Thakur, A. K.; Majumder, M.; Choudhary, R. B.; Singh, S. B. MoS_2 flakes integrated with boron and nitrogen-doped carbon: Striking gravimetric and volumetric capacitive performance for supercapacitor applications. *J. Power Sources* **2018**, *402*, 163−173.

(24) Xiong, P.; Ma, R.; Sakai, N.; Sasaki, T. Genuine Unilamellar Metal Oxide Nanosheets Confined in a Superlattice-like Structure for Superior Energy Storage. *ACS Nano* **2018**, *12* (2), 1768−1777.

(25) Pan, Q.; Zhang, Q.; Zheng, F.; Liu, Y.; Li, Y.; Ou, X.; Xiong, X.; Yang, C.; Liu, M. Construction of MoS_2/C Hierarchical Tubular Heterostructures for High-Performance Sodium Ion Batteries. *ACS Nano* **2018**, *12* (12), 12578−12586.

(26) Chen, C.; Xie, X.; Anasori, B.; Sarycheva, A.; Makaryan, T.; Zhao, M.; Urbankowski, P.; Miao, L.; Jiang, J.; Gogotsi, Y. MoS_2-on-MXene Heterostructures as Highly Reversible Anode Materials for Lithium-Ion Batteries. *Angew. Chem., Int. Ed.* **2018**, *57* (7), 1846−1850.

(27) Wang, R.; Wang, S.; Zhang, Y.; Jin, D.; Tao, X.; Zhang, L. Graphene-coupled Ti_3C_2 MXenes-derived TiO_2 mesostructure: promising sodium-ion capacitor anode with fast ion storage and long-term cycling. *J. Mater. Chem. A* **2018**, *6* (3), 1017−1027.

(28) Zhao, C.; Wang, X.; Kong, J.; Ang, J. M.; Lee, P. S.; Liu, Z.; Lu, X. Self-Assembly-Induced Alternately Stacked Single-Layer MoS_2 and N-doped Graphene: A Novel van der Waals Heterostructure for Lithium-Ion Batteries. *ACS Appl. Mater. Interfaces* **2016**, *8* (3), 2372−2379.

(29) Sun, T.; Li, Z.-j.; Wang, H.-g.; Bao, D.; Meng, F.-l.; Zhang, X.-b. A Biodegradable Polydopamine-Derived Electrode Material for High-Capacity and Long-Life Lithium-Ion and Sodium-Ion Batteries. *Angew. Chem., Int. Ed.* **2016**, *55* (36), 10662−10666.

(30) Zhang, L.-L.; Ma, D.; Li, T.; Liu, J.; Ding, X.-K.; Huang, Y.-H.; Yang, X.-L. Polydopamine-Derived Nitrogen-Doped Carbon-Covered Na3V2(PO4)2F3 Cathode Material for High-Performance Na-Ion Batteries. *ACS Appl. Mater. Interfaces* **2018**, *10* (43), 36851−36859.

(31) Clites, M.; Hart, J. L.; Taheri, M. L.; Pomerantseva, E. Annealing-Assisted Enhancement of Electrochemical Stability of Na-Preintercalated Bilayered Vanadium Oxide Electrodes in Na-Ion Batteries. *ACS Applied Energy Materials* **2020**, *3* (1), 1063−1075.

(32) Lakshminarayanan, R.; Madhavi, S.; Sim, C. P. C. *Oxidative Polymerization of Dopamine: A High-Definition Multifunctional Coatings for Electrospun Nanofibers - An Overview*; InTech: 2018.

(33) Zheng, W.; Fan, H.; Wang, L.; Jin, Z. Oxidative Self-Polymerization of Dopamine in an Acidic Environment. *Langmuir* **2015**, *31* (42), 11671−11677.

(34) Hu, X.; Yan, Z.; Li, Q.; Yang, Q.; Kang, L.; Lei, Z.; Liu, Z.-H. Graphene/vanadium oxide hybrid electrodes for electrochemical capacitor. *Colloids Surf., A* **2014**, *461*, 105−112.

(35) Chen, Z.; Augustyn, V.; Jia, X.; Xiao, Q.; Dunn, B.; Lu, Y. High-Performance Sodium-Ion Pseudocapacitors Based on Hierarchically Porous Nanowire Composites. *ACS Nano* **2012**, *6* (5), 4319−4327.

(36) Tepavcevic, S.; Xiong, H.; Stamenkovic, V. R.; Zuo, X.; Balasubramanian, M.; Prakapenka, V. B.; Johnson, C. S.; Rajh, T. Nanostructured Bilayered Vanadium Oxide Electrodes for Rechargeable Sodium-Ion Batteries. *ACS Nano* **2012**, *6* (1), 530−538.

(37) Wang, Y.; Alsmeyer, D. C.; McCreery, R. L. *Chem. Mater.* **1990**, *2* (5), 557−563.

(38) Huang, J.; Wang, Z.; Hou, M.; Dong, X.; Liu, Y.; Wang, Y.; Xia, Y. Polyaniline-intercalated manganese dioxide nanolayers as a high-performance cathode material for an aqueous zinc-ion battery. *Nat. Commun.* **2018**, *9* (1), 2906.

(39) Wangoh, L. W.; Huang, Y.; Jezorek, R. L.; Kehoe, A. B.; Watson, G. W.; Omenya, F.; Quackenbush, N. F.; Chernova, N. A.; Whittingham, M. S.; Piper, L. F. J. Correlating Lithium Hydroxyl Accumulation with Capacity Retention in V_2O_5 Aerogel Cathodes. *ACS Appl. Mater. Interfaces* **2016**, *8* (18), 11532−11538.